Atomic scale chemo-mechanics of silica: nano-rod deformation and water reaction

E.C.C.M. SILVA[a], J. LI[b,c], D. LIAO[b], S. SUBRAMANIAN[b], T. ZHU[d,e] and S. YIP[b,f,*]

[a]*Department of Civil and Environmental Engineering, Massachusetts Institute of Technology, Cambridge, MA 02139, USA*

[b]*Department of Nuclear Science and Engineering, Massachusetts Institute of Technology, Cambridge, MA 02139, USA*

[c]*Department of Materials Science and Engineering, Ohio State University, Columbus, OH 43210, USA*

[d]*Department of Mechanical Engineering, Massachusetts Institute of Technology, Cambridge, MA 02139, USA*

[e]*Department of Mechanical Engineering, Georgia Institute of Technology, Atlanta, GA 30332, USA*

[f]*Department of Materials Science and Engineering, Massachusetts Institute of Technology, Cambridge, MA 02139, USA*

Abstract. The notion of bond rupture as the initiation event leading to mechanical failure in a material system is well known. Less recognized but no less valid is that bond strain also fundamentally affects the chemical reactivity of the atoms involved in the bonding. This dual role of bond strain is clearly brought out in the present simulations. Stress–strain response of dry silica to the point of structural instability is studied using a classical inter-atomic potential model, whereas transition-state pathway sampling of water–silica reaction is performed using molecular orbital theory. Although not as accurate as possible from the standpoint of existing methods of simulation, the results nevertheless illustrate the physical insights into chemo-mechanical processes one can extract through multi-scale modeling and simulation.

Keywords: minimum energy path, molecular dynamics, molecular orbital, nanorod, silica, stress corrosion

1. Introduction

This paper provides a perspective on the molecular-level approach to understanding mechanical deformation, chemical reactivity, and their interactions as illustrated by silica in crystalline and disordered states, as well as in the form of a nanostructure. In addition to the intrinsic scientific merit of this problem class, the study is motivated by the current challenge to the broad community of disciplines that make up the rapidly emerging field usually called *computational science*. Some of the issues and motivations are discussed in the general Introduction to this collection of articles [72]. However, the combination of intrinsic scientific merit and complexity deserves particular attention in this section focused more on the study of physical systems (and less on methodology).

---

*To whom correspondence should be addressed, E-mail: syip@mit.edu

According to a recent report of the President's Information Technology Advisory Council [5], *computational science* is the use of advanced computing capabilities to understand and solve complex problems. It provides a unique tool (the near cliché is computational microscope) through which researchers can investigate problems that are otherwise impractical or impossible to address. That report implies, as do several studies commissioned by national funding agencies (particularly NSF and DOE), that appropriately complex problems are those which combine fundamental scientific interest with relevance to technologies of societal benefit.[1] The challenge – and opportunity – for computational scientists, therefore, is to formulate specific problems having sufficient breadth and depth that their exploration will expand the frontiers of *computational science*.

In this context, the present work may be viewed as a response from a particular project. Under the general framework of theory, multi-scale modeling and simulation (see the general Introduction [72]), we conduct a "bottom-up" study of silicon dioxide as an extension of existing studies on elemental metals (Cu) and semiconductors (Si) to a binary system of broad scientific and technological interest. We confined ourselves to two types of system responses, mechanical deformation to failure of bulk crystalline and amorphous silica as simulated by molecular dynamics, and water–silica reactions quantified by transition state pathway sampling using a semi-empirical molecular orbital model. The mechanics issues are considered from the standpoint of theoretical strength of materials, while the reactivity aspects are examined in terms of mechanisms of hydrolytic attack on quartz. The work is part of the coordinated Information Technology Research project focused on the intersection of chemistry, materials physics, and the mechanics of materials. The single, paradigmatic problem under study is the chemo-mechanical behavior of the silica–water system.

The basic notion underlying this perspective is that deformation and reaction processes are fundamentally governed at the molecular level by an inter-atomic bond exceeding its stability limit. We induce such an instability by subjecting the system to a uniform loading, generating a stress–strain response. When the response shows an extremum, a structural change in the system is indicated, the significance of which can be assessed by detailed study of the atomic configurations before and after the change. Thus, atomistic simulations provide a direct route to correlation of the local information of the state of a particular inter-atomic bond in the system with the overall mechanical and chemical behavior of the system. Section 2 begins with a brief summary of how the inter-atomic interactions are treated in simulations, followed by a discussion of deformation of bulk silica in the dry state in Section 3. In Section 4, we consider the silica nano-rod, also studied in this collection by Muralidharan et al. [55] and discuss its deformation behavior. We then present the main results of this study, namely the reaction of a strained nano-rod with water. It will be seen in Section 2 that we use a classical empirical inter-atomic potential for all the deformation simulations, and a simple form of molecular orbital theory when reaction with water is being treated. At the present stage of exploratory studies, and in the context of the earlier papers in this collection by our colleagues, we do not view it as justifiable to use the most accurate (and generally heavily parameterized) descriptions possible for the inter-atomic interactions. At the same time, we will refrain from

---

[1]See the report of the NSF Blue Ribbon Panel, Simulation-Based Engineering Science [60].

attributing anything more than qualitative (or at most semi-quantitative) significance to the results presented here. In addition to inter-atomic interactions, we also discuss in Section 2 the sampling of reaction pathways to determine the minimum energy path. From it one extracts the reaction coordinates and the activation barrier. In the following section, bulk deformation of silica is investigated in both crystalline (α-quartz) and amorphous states under various modes of loading. In Section 4, we switch to the silica nano-rod as a reference structure for the study of water interaction, the most complicated situation considered. The determination of reaction pathways for water–silica reaction, along with the activation barrier as a function of bond strain, serve to illustrate the advantages and limitations of current capabilities for addressing problems that involve mechanical deformation and chemical reaction. This is of course only one of the first steps toward unraveling the complexity of the water–silica system.

2. Modeling concepts and simulation techniques

The underlying principle of multi-scale materials modeling and simulation is the description of the system of interest across several characteristic length and time scales [72, 89]. In the bottom-up implementation, the primary degrees of freedom of the system are those associated with the atoms and electrons that comprise the system. If the atoms as structureless objects (i.e., without distinguishing nuclei and electrons) are sufficient to describe the problem under consideration, one may treat the electrons implicitly and resort to classical atomistic simulations to track the atoms as driven by classical inter-atomic interaction potentials. Preceding papers in this collection [47, 55, 95] discuss such potentials and their parameterization in detail. The advantage of this approach, which we adopt in the study of mechanical deformation, is that the constraint on the number of atoms that can be handled is not severe. On the other hand, if electronic effects have to be taken into account explicitly, such as in the analysis of water–silica reaction, then quantum mechanical (QM) methods, which are much more computationally demanding, have to be applied. See also the discussion in the general Introduction on linking quantum mechanical and classical simulations [4, 37, 72] in this collection.

2.1. CLASSICAL EMPIRICAL POTENTIAL (BKS)

The empirical potential used in our mechanical deformation studies is the two-body BKS form already discussed at length in this collection [47, 55, 95]. Recall that it is comprised of the electrostatic interaction between two point charges and short-range interactions of the Buckingham form [81]. For atoms i, j separated by r_{ij}, it reads

$$V_{ij} = \frac{q_i q_j}{r_{ij}} + a_{ij} \exp(-b_{ij} r_{ij}) - \frac{c_{ij}}{r_{ij}^6}, \qquad (1)$$

where both the atomic charges q_i, q_j and the coefficients a_{ij}, b_{ij}, and c_{ij} are parameters. By comparison with data from relatively low-level ab-initio calculations on H_4SiO_4, the Si–O bond stretch was used to determine the Si–O interaction, while the O–Si–O angle bend was used to fix the non-bonding O–O interaction. The remaining ambiguity in the parameters was eliminated by fitting to the the experimental lattice

Table 1. Parameters for the BKS potential (Eq. (1))

$i-j$	a_{ij} (eV)	b_{ij} (Å)	c_{ij} (Å^{-1})	Charges
Si–O	18003.7572	4.87318	133.5381	$q_{Si} = 2.4$
O–O	1388.7730	2.76000	175.0000	$q_O = -1.2$

Note: For Si–Si pairs, only Coulombic interactions are considered

parameters and elastic constants of α-quartz. Again, consult the earlier papers in this collection. For the parameter values used see Table 1.

This two-body interaction description has been used to study crystalline silica, including α-quartz [64], as well as amorphous silica [18]. The same set of parameters was able to reproduce the experimental unit cells and elastic constants of four other silica forms, α-cristobalite, coesite, stishovite and silicalite [81]. Both tetrahedral and octahedral forms of crystalline silica are represented in this set. Amorphous silica also is described reasonably in terms of density, radial distribution function, and distribution of bond angles and bond lengths [88]. On the other hand, the potential does not allow the atomic charges to vary, and polarizability and three-body effects are ignored. One has other alternatives in that core-shell polarizable models [15, 65], variable charge potentials [56] have been proposed, along with three-body interactions [19, 82]. For a recent review of the silica potentials used in the simulation of glass fracture, see [56].

2.2. SEMI-EMPIRICAL MOLECULAR ORBITAL METHODS

Semi-empirical QM methods are electronic structure methods of particularly simple form, typically based on Hartree–Fock theory. The virtue of such methods is computational simplicity. Recall the discussion by Bartlett et al. earlier in this collection [4]. This simplicity is achieved by treating the core electrons together with the nuclei and using a minimal basis set of valence orbitals. Computational efficiency is gained thereby at the cost of lower accuracy relative to true ab-initio methods. In the neglect of diatomic differential overlap (NDDO) approximation, the Hartree-Fock energy expression is simplified by omitting integrals involving diatomic differential overlap. The remaining integrals, as well as the interaction between cores, are calculated using approximate expressions involving empirical parameters. The result of the calculation is a set of molecular orbitals, given as a linear combination of a basis set of valence shells. From these orbitals, the electronic energy of the system can be calculated and added to the core interaction energy, giving the total energy of the system. Ionic charges also can be calculated, and charge transfer does take place.

In this work, we used the NDDO semi-empirical methods known as PM3, and PM5, which are available in the commercial code MOPAC2002 [66]. These methods are parametrized for most major elements and elemental pairs using experimental data. The accuracy of semi-empirical calculations is largely governed by the approximations mentioned above. The PM5 method is able to predict the heat of formation of 79 compounds containing Si [66] with an average error of 6.6 kcal/mol, comparable to the error in density functional theory (DFT) calculations. There is less

information on the accuracy in determining transition states and activation barriers. In the problem of hydrolysis of silica, PM3 and DFT results were found to be qualitatively similar [43].

2.3. TRANSITION STATE THEORY

Under quasi-static loading at $0\,K$, failure occurs at the critical (or athermal) load, when the activation barrier for the failure process vanishes. The structure will deform continuously until this load is reached, at which point failure occurs by a sudden transition to a lower-energy, stable final state. However, since the energies of the initial and final states are stress-dependent, it is possible that the transition to the final state becomes thermodynamically favorable before the critical load is reached. In that case, only an activation barrier prevents the system from instability. Depending on the temperature and time scale of the simulation, it may be very difficult to observe the transition without overdriving the system. An alternative method that can lead the system gradually up the activation barrier through the saddle point and toward the final configuration would be quite desirable.

Our study of the stress-dependent water–silica reaction was carried out within the framework of Transition State Theory (TST) (e.g. [83]). The problem becomes that of identifying the reaction mechanism and finding the free energy barrier. Within the harmonic approximation to TST, it is sufficient to find the Minimum Energy Path (MEP) on the (electronic) adiabatic potential energy surface (PES). The MEP is defined as a continuous path in a $3N$ dimensional configuration space, where N is the number of atoms, such that the atomic forces at each point are zero in the $3N-1$ dimensional hyperplane perpendicular to the path. The maximum energy along that path defines the saddle-point and the activation barrier. We used a reaction pathway sampling procedure, the Nudged Elastic Band (NEB) method [30, 36], to determine the MEP, and consequently the reaction mechanism and activation barrier. The evolution of the PES with stress manifests itself as a stress-dependent activation barrier.

3. Deformation of bulk silica

In this section, we establish the basic structural failure behavior of silica, in crystalline form as α-quartz and and in an amorphous form, when subject to large compressive and tensile strains. Our interest is to examine the nonlinear stress–strain behavior in the vicinity of structural instabilities, as observed by direct molecular dynamics (MD) simulation. At the same time, we will interpret their characteristic features in terms of deformation modes and local structural environment in each case.

All simulations were classical MD using the BKS potential and a simulation cell with periodic boundary conditions. System temperature was fixed via the Nosé–Hoover thermostat [34, 58]. For constant stress MD (Section 3.1.1), we used Parrinello–Rahman [62] MD at 300 and 1073 K, in periodic simulation cells with 192 SiO_2 units (576 atoms) for hydrostatic deformation, 384 units (1152 atoms) for uniaxial loading on the x- direction and 480 units (1440 atoms) for uniaxial loading on the c axis. At each state point on the stress–strain curve, the system was equilibrated for 10 ps and run for 5 ps, followed by static relaxation and the strain was measured with this equilibrium structure.

Strain-controlled simulations (Section 3.1.2) were performed in a cell containing 5184 atoms. Each unit vector of the simulation cell was about 4 nm, corresponding to a total of 576 unit cells of α-quartz. System temperature was held at 300 K. Loading was applied through incremental strain on the simulation cell at a rate of 5×10^{10} s^{-1} for each given loading direction.

3.1. α-QUARTZ

3.1.1. *Stress-controlled deformation*

Previous work on structural transitions and properties of SiO$_2$ have focused on the phenomenon of pressure-induced amorphization and the related crystal–crystal transformations in quartz prior to amorphization [12, 57, 73, 74, 76, 77]. By contrast, there have been comparatively few simulations of uniaxially compressive loadings on any structure [38, 39, 79, 80]. Simulations of uniaxial deformation behavior at high stresses and high temperature are of interest from the standpoint of understanding the plastic deformation of quartz, particularly given the extensive experimental data [2, 3, 10, 11, 13, 14, 32, 33, 63]. In our simulations, as with many of these experiments, a confining pressure (1.55 GPa) and a high temperature (1073 K) were chosen to probe the plastic deformation of quartz crystals without incurring any faulting. Some of the results have been discussed previously [67, 68]. We summarize the main points and add some previously unpublished results.

Multiple studies [1, 6, 7, 12, 57, 69, 73–76, 85] have shown that the BKS potential is able to account for structural phenomena in SiO$_2$ such as the pressure-induced amorphization and elastic instability observed in quartz [6,7,73], the properties of the evolved amorphous structure [74], the intermediate crystal–crystal transitions that exist before amorphization [76], the mechanism of this amorphization [85], other new stable structures [1, 69, 75], and the structure and phase transformations of other silica polymorphs [57, 75]. This gives us confidence that the BKS potential is adequate for this level of study.

First, we verified that the simulated hydrostatic stress–strain response at 300 K for a defect-free single crystal quartz, shown in Figure 1, agrees with previous simulations [6, 7, 12, 73, 74] and experiment [29]. Our results are consistent with the pressure-volume curve given by Tse and Klug [73]. The strain increases with applied stress up to around 19 GPa, whereupon the lattice becomes unstable and transforms to an amorphous structure. The amorphous character was confirmed by inspection of the atomic configuration and comparison of the radial distribution function (RDF) with that of amorphous silica. A discontinuity in the strain response marks this amorphization. Further increase of pressure after the point of instability results in a corresponding strain increase in the amorphized structure.

Next, we simulated the uniaxial stress-strain response at a temperature of 1073 K. The loading condition was such that there was a constant pressure of 1.55 GPa on the background and a uniaxial loading on the x-direction, perpendicular to the (10$\bar{1}$0) plane in quartz, or on the c axis, perpendicular to (0001) plane in quartz. These directions of loading are denoted by $\perp m$ and $\|c$, respectively, in experiments [11, 13, 14]. The stress recorded on the uniaxial scale is the differential stress over the confining pressure applied, following the convention used in experiment [78]. The resulting stress–strain curve is shown in Figure 1 for both deformation directions.
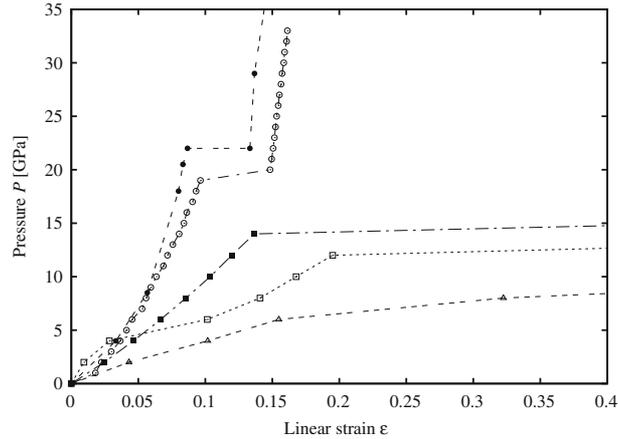
Figure 1. Simulated stress–strain response of α-quartz, under controlled stress conditions. Hydrostatic or differential pressure is plotted against the linear strain ε. (○) Hydrostatic compression at 300 K, (●) results by Tse and Klug [73], (■) uniaxial compression in the x-direction at 1073 K, (□) uniaxial compression in the c direction at 1073 K, and (△) uniaxial deformation of amorphous silica. Note the large discontinuities in the strain response when the pressure-induced amorphization occurs. The discontinuity, when loading up to 6 GPa on the c-direction, is a stacking fault.

When loaded on the x-direction, the crystal responds linearly until about 14 GPa. Upon release of the uniaxial stress, the crystal structure at 14 GPa returns almost completely to a α-quartz structure. Although this type of response may not be observed in single crystals with a finite dislocation density, it gives the upper limit to elastic deformation before some form of failure. Similar results were obtained for the c direction, except for the generation of a stacking fault in the basal plane between 4 and 6 GPa. When loaded in this direction, failure occurs at a lower stress (12 GPa). The strength of the basal planes, perpendicular to the loading direction, are known to be the lowest, therefore we can expect this loading direction to be the weakest for α-quartz.

When loaded above its uniaxial strength, the crystal structure collapses, leading to a time-dependent evolution of an amorphized structure. This behavior was confirmed by comparing the RDF and the atomic configuration of the structures, before and after the discontinuity, with our own simulated amorphous SiO_2 and with the literature [61]. The mechanism of amorphization was studied by examining the atomic configurations during the relaxation period. At 1.2 ps, it was observed that a planar column of atoms perpendicular to the compression direction have disordered, while the rest of the crystal structure remains ordered. At 1.6 ps, the amorphization has spread to one half of the simulation cell, while the other half of the cell still retains periodicity to some extent. After 2.5 ps, the whole cell was amorphized. By contrast with hydrostatic simulations, where the failure was homogeneous throughout the simulation cell, under uniaxial compression we observed an anisotropic nucleation and growth mechanism leading to layered amorphous structures in the crystal.

We believe that this structural change signals a lattice instability similar to that observed by other investigators [6, 7, 12, 73, 74] under different loading conditions. The instability can be regarded as a failure of the material in the direction of compression, such that the lattice no longer can withstand higher pressures past

this point, and collapses. In constant strain or constant volume simulations, this corresponds to the lowering of measured stress beyond the maximum point, signaling the point of failure [59].

For comparison, Figure 1 also shows the simulation result for an amorphous SiO_2 structure loaded uniaxially with the same confining pressure. As could be expected from hydrostatic results, a-SiO_2 transforms continuously to flatter or layered structures under uniaxial loading. One can see clearly that the strength of amorphous structure is significantly lower than the crystal structure under corresponding loading geometries, for simulation runs under similar conditions. This explains the very large deformations after amorphization of crystalline quartz.

Experimental studies on uniaxial compression in quartz crystals or aggregates are extensive. Features such as deformation lamellae, bands, undulatory extinction [11], faulting along particular planes, isotropic glassy zones [14], and recrystallization [32] and anomalous high strength have been recorded in these experiments. Here we will consider two such features (fracture planes and glassy zones) in the context of our simulation results.

The quartz crystal structure falls in the trigonal-hexagonal lattice type with α-quartz having a $P3_121$ space group. The slip planes for hexagonal lattice type are given by $\{0001\}$, $\{10\bar{1}0\}$, $\{10\bar{1}1\}$ and the slip directions by $\langle a \rangle$ or $\langle a+c \rangle$. Out of these, the $\{0001\}$ basal slip is observed most commonly. When plastic deformation was first recorded in quartz crystals [10], it was observed that the crystals had predominantly slipped in the basal plane $\{0001\}$ [11, 13] as slip along this plane requires lower shear stress than other slip planes.

Christie et al. [14] have made experimental deformation studies of quartz at room temperature. The samples failed by sudden rupture, with a rapid decrease of pressure. They reported many fractures with different orientations and primarily planar structures. We highlight here two types of fracture: *slip assisted* fracture, developed from shear stresses, and *instability assisted* fractures ("other planar fractures" in the original), which we suggest to be due to compressive stresses which lead to instability. Christie et al. claim that slip-assisted faults, which had a strong tendency for parallelism with operating slip-planes of quartz, were formed because the faulting itself was initiated by small amounts of slip on these planes; this would give rise to submicroscopic cracks which become large enough to propagate as brittle fractures. However, instability-assisted fractures, unlike the faults, showed no displacements or sheared zones along the fracture plane, which were planes of zero shear stress during loading, normal to the axes of maximum principal stress. These fractures showed a rather weak tendency of parallelism with possible operating slip-planes.

Our stress-controlled simulations suggest that, when compressive stresses reach beyond the point of stability of the lattice, a layered or near-planar block of a denser amorphous structure is formed perpendicular to the applied stress direction, through a nucleation and growth mechanism. While we do not give here a full mechanism leading to fracture, it is conceivable that in real experiments, since an inhomogeneity in structure and stresses is created around the amorphized zone, the material will fracture along this plane, possibly during the unloading of the sample. This type of failure can be directly observed in situations where the compressive stresses are not relieved by any slip-assisted failure prior to the instability-assisted failure. Some examples are ideal quartz crystals with no dislocations or defects that could aid

slip-assisted failures, regions of a crystal with very low dislocation and defect density, and crystals loaded in a direction perpendicular to the primary slip system, which preempts slip-assisted failure.

It should be noted however, that when the material just slips without failing (or fracturing), only the shear stresses are relieved, and the compressive stress is still active perpendicular to the slip system. This behavior could lead to the same failure through amorphization described above, with the layered structure described being oriented this time along the active slip system. This distinction may explain the observation of thin zones of isotropic (glassy) material along the fracture surfaces in these experiments, an observation which could not be explained clearly from slip and fracture considerations alone, or from other possible explanations such fusion or mechanical disruption along slip planes. Further experimental clarification about these phases is still required.

3.1.2. *Strain-controlled deformation*

This section focuses on the behavior to failure, under strain control, for hydrostatic and uniaxial compression, and uniaxial tension. Figure 2 shows the stress–strain curve in the case of hydrostatic compression. Typical linear response is seen initially with change to nonlinear in a concave manner beyond ∼5% strain, displaying increasing resistance with deformation. With further strain, the pressure shows a sudden drop, at point (a), indicating a structural instability. Apparently the system has found a particular structural arrangement at a significantly lower stress level, from about 26–15 GPa. Without examination of the actual atomistic configurations, one would not know a priori what specific structural rearrangement has occurred. As strain loading continues, the system pressure again rises and goes through a series of small oscillations (suggestive of slight, local structural changes with corresponding stress relaxation) before reaching a second, pronounced drop at point (b). Thereafter, the response curve rises more or less smoothly with increasing loading.

To see what structural rearrangements occurred at (a) and (b), one can follow the evolution of the atomic configurations produced during the simulation. We find
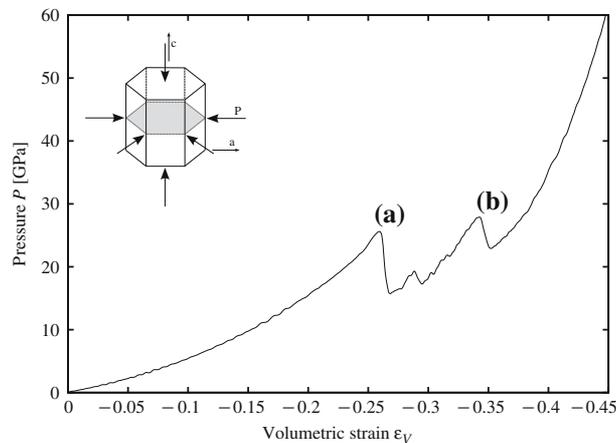

Figure 2. Stress–strain curve for uniform compression of α-quartz at 300 K. (a) Crystal–crystal transition and (b) amorphization. Inset: crystalline axes.

the crystal lattice deforms uniformly up to point (a), when an atomic layer perpendicular to the c axis transforms into a different crystalline structure. This transformation causes the overall strain to be localized with accompanying stress reduction. Between points (a) and (b) additional layers are transformed. At point (b), the interfacial region between the original and the new crystalline structures collapses, driving the entire structure into a disordered state. By unloading from different points, we could verify that the deformation is elastic until (a). Between (a) and (b), immediate unloading caused the system to return to α-quartz, showing that the transformation is reversible.

Since quartz is anisotropic, uniform strain generates a non-hydrostatic stress state, with the higher normal stress along the c-axis. The sample undergoes a phase transformation to a second crystalline phase when $P_{conf} = 21.8$ GPa ($P_{diff} = 11.6$ GPa). The differential load at failure and the failure plane are similar to that observed in stress-controlled uniaxial deformation along the c axis. In the strain-controlled simulation, it is possible to visualize the localization of strain in layers perpendicular to the c-axis, stress relaxation in this direction, and reduction of the differential pressure. Si atoms are penta- and hexa-coordinated, suggesting that this structure may not be the same one observed previously [9, 67, 77]. The regions eventually consolidate and the material undergoes a second transition at the confining pressure $P_{conf} = 31.3$ GPa (differential pressure $P_{diff} = -9.9$ GPa), where atoms in a layer of this new crystal become disordered. Again the differential stress was reduced. Since the amorphous material is anisotropic, the differential stress develops with continued deformation. Further consolidation (not shown) leads to an isotropic amorphous material. Return curves show that the crystal–crystal transition is reversible, while the amorphization is irreversible. It is also seen that the amorphous phase is consolidating irreversibly.

Many phases have been experimentally observed after hydrostatic compression of quartz, and metastable states may predominate under different loading histories. Pressure-induced amorphization in quartz quenched from 30 GPa was observed by Hemley [28]. The resulting structure exhibited a degree of anisotropy, as observed by McNeil and Grimsditch [50], whereas a quenched melt is isotropic. Kingma et al. [40, 41] observed that pressure-amorphized samples from 22 to 30 GPa had a phase transformation prior to amorphization, at around 21 GPa, and a return to a quartz-like structure on unloading, suggesting memory effects on quartz. Beyond 30 GPa, the crystal had fully amorphized into an anisotropic phase. During compression, amorphous lamellae are formed.

In simulation, BKS α-quartz becomes unstable around 20 GPa, when pressure-induced amorphization occurs either directly [68, 74] or through intermediate crystalline phases [73, 77]. Campañá et al. [9] showed that amorphization can be avoided up to at least 50 GPa. Those simulations were pressure controlled, allowing for abrupt transitions between the phases. In this section, we performed simulations under uniform controlled strain in order to observe the evolution of the amorphization process and analyze intermediate states of change.

The behavior under strain-controlled uniaxial loading in the a direction is shown in Figure 3. The system deforms elastically until point (a), where instability leads to the formation of bands parallel to the ($10\bar{1}1$) plane, and to stress relaxation in the loading direction. Notice that slightly convex non-linear behavior sets in at larger strain relative to the response to hydrostatic compression. Subsequent deformation
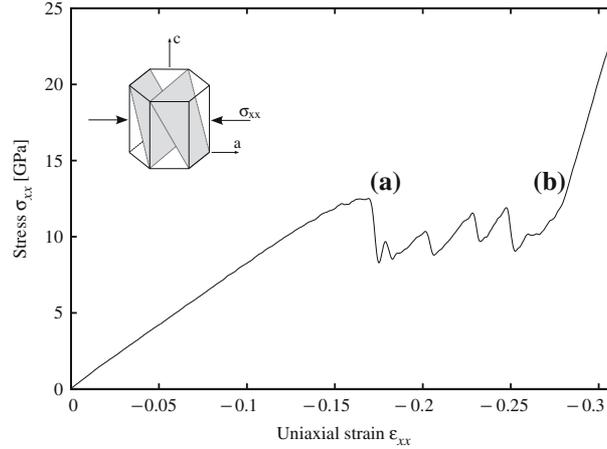
Figure 3. Stress–strain curve of α-quartz under strain-controlled uniaxial compression on the a axis. (a) Beginning of the first crystal–crystal transformation, (b) end of the first transformation. The $(10\bar{1}1)$ plane is highlighted.

occurs by stepwise thickening of these crystalline bands, until the whole system is transformed into the new phase, approximately at point (b). This new phase is stable and deforms elastically. Similar behavior is observed for loading in the c direction.

Differential compression commonly is employed to induce dislocation nucleation and observe the hydrolytic weakening in wet quartz [16]. Unconfined uniaxial compression results in cracking, except for very high water contents or temperatures above 1000 K. Under the range of confining pressures in the literature (up to 1.5 GPa), dry quartz always fails mainly through microcracking and layered amorphization. The slip planes are the basal plane (0001), the prismatic plane $\{10\bar{1}0\}$ and the $\{10\bar{1}1\}$ plane. Dislocations, amorphization and fracture are observed in these planes, as well as $10\bar{1}n$ with small n. Loading is usually applied at 45° to the a and c-axes (the O^+ direction) or in the $[10\bar{1}1]$ direction.

Figure 4 shows the stress-strain behavior of BKS quartz under uniaxial tension in the a direction (analogous behavior is observed in the c direction). The kink at low strains corresponds to the α-to-β transition of quartz [45]. As before, deformation is elastic and uniform until the system becomes structurally unstable. In this case, failure occurs by a sudden opening of an atomic-sized crack perpendicular to the loading direction.

In summary, the behavior of crystalline silica reflects its ordered structure. The crystal deforms elastically and uniformly until a global instability point is reached. At that point, the structure seeks a lower energy state, which can be an alternative crystalline form or a disordered state. The instability mode will depend on the loading type. In compression, we observe a progressive polymorphic transformation, whereas in tension we find the nucleation of a single crack.

3.2. AMORPHOUS SILICA

Amorphous silica or silica glass is an important metastable form of silica, composed of a random network of corner-sharing silica tetrahedra (SiO_4). Its disordered
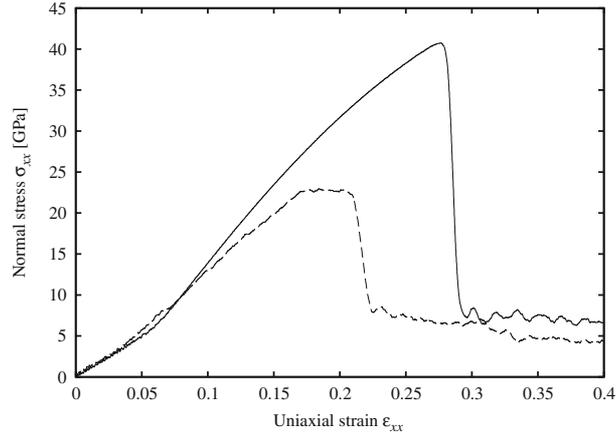
Figure 4. Stress–strain curve for uniaxial tension of α-quartz along the *a* axis.

structure gives rise to distinct mechanical properties and behavior relative to the crystalline varieties. Since the system is heterogeneous, in that there are regions of relative order as well as highly disordered regions, one should expect that the system becomes locally unstable before macroscopic failure.

Amorphous simulation samples were produced by heating cristobalite samples to 6000 K through velocity scaling, equilibrating for 7.5 ps, and cooling to 300 K at a rate of 2×10^{10} K/s, while keeping the volume at the density of cristobalite (2.16 g/cm^3), and relaxing at the end to zero pressure. This process yields final densities between 2.30 and 2.32 g/cm^3. The resulting structure is tetra-coordinated with few defects, and the radial distribution function correlates well with other BKS silica glasses. Compare also the discussion by Muralidharan et al. [55].

Figure 5 shows the stress–strain curve of amorphous silica under strain-controlled hydrostatic compression. Compared to Figure 2, the response varies monotonically with no sudden instabilities. From the unloading curves, it is clear that residual strains are being stored at a level that is proportional to the loading. Thus the amorphous behavior stands in sharp contrast to the crystalline response, the system is weaker in strength, and deformation is more distributed. Another significant aspect, which we note but do not address in any detail, is rate dependence. It is to be expected that the amorphous system will have longer relaxation times relative to the crystal, which makes the simulation study more sensitive to the kinetics of the deformation and relaxation processes.

In Figure 5, the response is elastic up to about 5 GPa, beyond which compaction proceeds progressively and irreversibly, as shown by the unloading curves, down to 70% of the original volume. Compression occurs through local transitions between regions of lower and higher density, occurring at different points in the sample.

Experiments show that amorphous silica densifies under hydrostatic pressure, and that the dense phase is maintained at room temperature. Mukherjee et al. [54] observed a first-order transition (from amorphous to amorphous). The observed density was 2.24 g/cm^3 at 4 GPa, 450°C (before the transition), and 2.54–2.58 g/cm^3 after heating above 700°C. The phase transition was accompanied by a 20% volume change that occurred at 3.6 GPa for 680°C. Crystallization was observed at
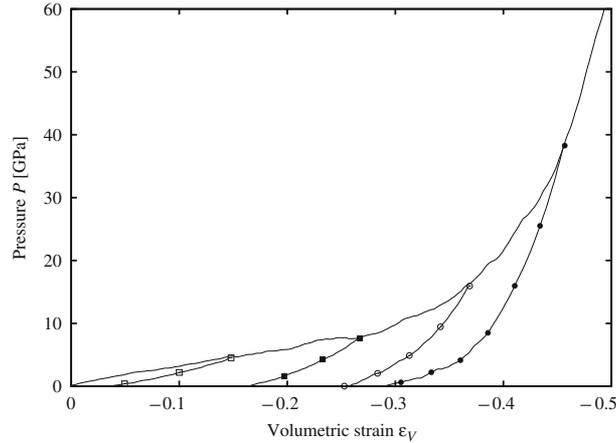
Figure 5. Pressure versus volumetric strain for strain-controlled uniform compression of amorphous silica. (–) Loading curve and (○, ●, □, ■) unloading from different points.

high pressure (e.g., 4 GPa at 800°C), meaning that the glass transition temperature is pressure-dependent.

Lacks [42] had suggested that a first-order amorphous-to-amorphous phase transition exists in silica at 3 GPa, but that it is kinetically hindered in both MD and experiments. Indeed, the transition occurs gradually in MD from 6 to 40 GPa, and 8 to 25 GPa in experiments. Mukherjee et al. [54] were able to observe the transition by performing the experiments slightly below the glass transition temperature. This high-density amorphous silica is still tetra-coordinated in simulation and experiment.

El'Kin et al. [18] proposed a non-equilibrium phase diagram for a-SiO$_2$, taking into account their own experiments and the existing literature. Three distinct amorphous phases were proposed, the two tetrahedral phases and a high-density phase composed of [SiO$_6$] octahedra.

Figure 6 shows the stress–strain behavior of amorphous silica under strain-controlled uniaxial tension. It can be seen that the strength of amorphous silica is much lower than that of α-quartz, and that the amorphous system displays some plastic deformation before failure. Swiler et al. [70] observed that fracture occurs through growth and coalescence of voids. Liao [45] divided the failure process in four stages: (i) elastic, where voids grow reversibly, (ii) void nucleation, (iii) void growth and coalescence, and (iv) void extension as a crack.

Our results indicate that amorphous silica deforms and fails in a very different manner than does crystalline silica. Any representative sample will have a wide distribution of bond lengths and bond angles, therefore the local state of strain will be very different at various points. This distribution is reflected in the deformation and failure modes, which occur through several small local events. Each local domain relieves its own stress through local rearrangement and densification (under compression) or bond breaking and void formation (in tension), while the system as a whole is still able to resist the global stress.

The behavior of a simulated amorphous sample will be sensitive to these local events, a factor that increases in importance as the sample becomes smaller. Therefore, choosing a representative sample and extrapolating its behavior to the bulk is less straightforward than in the crystalline case.
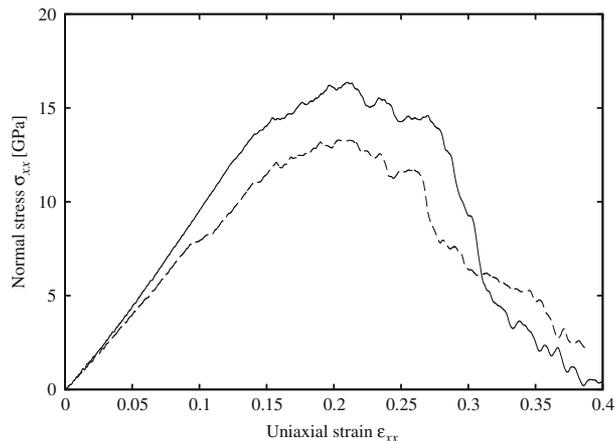
Figure 6. Stress–strain curve for uniaxial tensile deformation of amorphous silica, intact (solid line) and pre-cracked (dashed line).

4. Nano-rod deformation and water reaction

The present study of deformation-driven failure of a nanostructure in the form of a free-standing rod and the reaction with water of such a structure is motivated by a simple notion, namely, both chemical and mechanical behavior of materials at the atomic level are fundamentally controlled by the action of the inter-atomic bond. In other words, bond strain not only determines mechanical deformation, it also affects chemical reaction. To quantify this notion we turn to an appropriate structure which is small enough for atomistic simulation but scalable to bulk matter in terms of meaningful measures of stress and strain. The nano-rod which we adopt here is one system which satisfies this requirement.

As discussed in the work by Mallik et al. in this collection [47], the 108-atom silica nano-rod (Figure 7) is formed by a stack of four rings of corner-sharing silica tetrahedra, capped by two rings of edge-sharing tetrahedra. The resulting structure has the SiO_2 stoichiometry and is free of dangling bonds without artificial saturation.
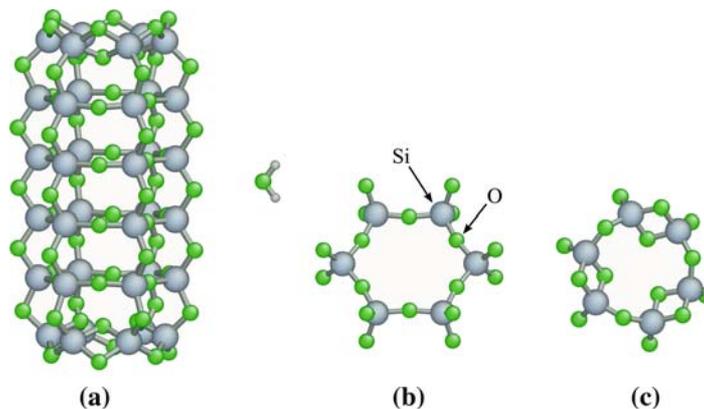

Figure 7. Nano-rod structure. (a) Full 108-atom nano-rod and a water molecule, (b) corner-sharing internal rings, (c) edge-sharing end ring. Larger atoms are silicon and smaller atoms are oxygen [92].

The size and geometry of the nano-rod are similar to the channels in α-quartz, and its outer wall resembles the (0001) surface of this mineral, where all Si and O atoms are fully coordinated.

Currently it is not possible to study the water reactions that cause stress corrosion and hydrolytic weakening using solely classical MD. Work in that direction [15] still needs to be validated against electronic structure calculations.

Here the energy and force calculations were carried out using the BKS potential as well as the semi-empirical QM methods, PM3 and PM5. Even with those methods there is a need for small but representative structures, which may be treated with QM methods. Work on very small clusters [46] and rings [86] provided information about the silica–water reaction, but correlation with bulk material behavior was not attempted. The nano-rod [94] may be the simplest small structure for which a meaningful stress state can be defined. Its deformation behavior in tension is analogous to that of crystalline silica, serving as a model for stress-induced water reaction in these materials. Similarly, small periodic cells containing amorphous silica have been used as models for DFT simulation of amorphous systems [21, 22].

4.1. Deformation behavior of a dry nano-rod

We deformed the nano-rod in tension and compression by prescribing the axial displacement of the six Si atoms at each end ring, and allowing the remaining atoms to relax [90]. This deformation corresponds to a quasi-static, strain-controlled experiment at 0 K. Each step of incremental strain consists of scaling all the atomic positions to impose the prescribed strain, holding the end atoms fixed, and letting the whole system relax by minimizing the energy. The gauge length used to define strain was the distance between the two end rings, which were kept parallel, divided by the initial length l_0. The nominal cross-section, used to define stress, is therefore $A_0 = 4\pi d_{OO}^2 = 88.9$ Å^2, where d_{OO} is the side length of a SiO$_4$ tetrahedron; it is also the edge of the hexagon formed by the six bridging oxygens in the planar rings. The same area was used in all tension and compression studies (classical BKS or semi-empirical QM PM3 and PM5).

The stress–strain response of the nano-rod is shown in Figure 8. As we have seen previously [94], during tensile deformation all Si–O–Si (siloxane) bonds are equally stretched and reach the instability point almost simultaneously. Once the first bond breaks, strain localization occurs at that site to nucleate a fractured state (Figure 9b). This is essentially the same process observed in bulk quartz, with the magnitude of the critical stress being similar in the two cases.

The configurational details reveal that instability occurs in compression by buckling, as shown in Figure 9d, which is reasonable in view of the large aspect ratio. This deformation mode is quite distinct from that of bulk silica. Further compression induces rearrangement of the nano-rod structure, behavior which is not expected to be analogous to the phase transformations induced in bulk quartz.

4.2. Deformation behavior in the presence of water

Chemical reaction rates in solids are known to be sensitive to the stress level in the system (e.g. [20, 31, 44]). This effect can be characterized by the variation with stress
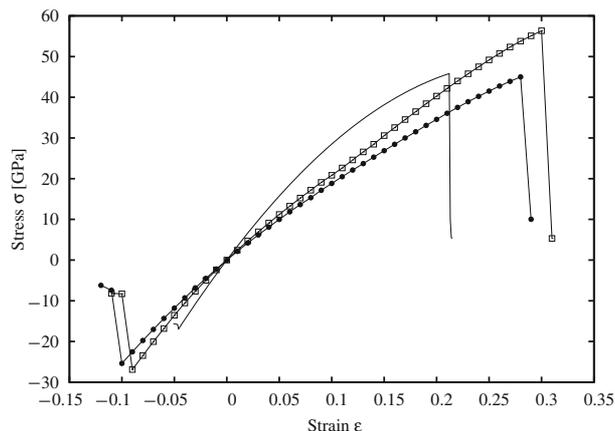
Figure 8. Stress–strain curve of a dry nano-rod in compression and tension until failure, for different computation methods: (–) classical MD with the BKS potential, (□) semi-empirical PM3, (●) semi-empirical PM5.
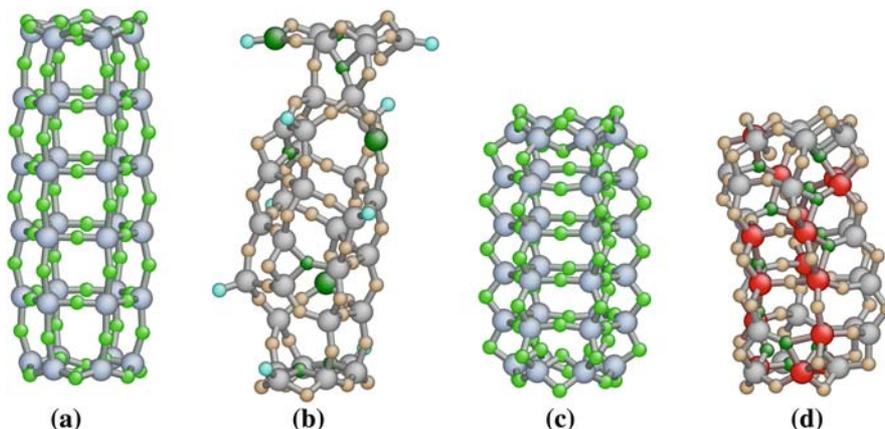

Figure 9. Failure of the nano-rod simulated using the PM5 QM semi-empirical method, in tension and compression. (a) Last stable structure in tension and (b) failure mode. (c) Last stable structure in compression and (d) buckling failure mode. These modes are representative of the other methods. Highlighted atoms are over- or under-coordinated.

of the activation barrier for the reaction. A typical example is stress corrosion of silica glass in the presence of water; the strength of glass placed under a static load in an aqueous environment decreases with time [87]. The phenomenon, known as delayed failure or static fatigue, refers to the slow growth of pre-existing surface flaws as a result of corrosion by exposure to water. From the microscopic standpoint it is believed that water molecules will attack the strained siloxane (Si–O–Si) bonds at the crack tip, causing bond rupture and formation of terminal silanol (Si–OH) groups which then repel each other [52, 53]. This is the molecular-level mechanism that governs intrinsically the macroscopic kinetics of quasi-static crack motion.

A full understanding of stress corrosion in silica glass also must consider quantifying reaction kinetics by mapping out the reaction pathways and determining explicitly the activation energies. In the case of vitreous silica, the chemical reaction between

the intrusive water molecule and strained siloxane bonds is envisaged to proceed in three steps, adsorption, reaction, and separation [52, 53]. Further, it was suggested [51] that bond-angle deformations are very effective in enhancing chemical reactivity. In particular, stress-induced pinching of the O–Si–O bond angle can form a chemically active kink site. Besides direct deformation of a siloxane ring, the calculated reactivity of various cyclosiloxane rings has been compared to deduce reaction pathways for three and four fold silica rings and a five fold ring-chain structure [86]. Such information also is useful in understanding the kinetics of hydrolyzing the silica surface, in which various types of ring structures can exist as a result of surface reconstruction [17, 84].

In this work we consider an idealized model of stress-induced hydrolysis reaction, in which a single water molecule interacts with the silica nano-rod, which we have just discussed in the dry state. It will be seen that three competing hydrolysis reaction pathways can be identified, each involving a distinct initiation step. The processes are water dissociation, molecular chemisorption, and direct rupture of siloxane bond, which dominate at low, intermediate, and high stress levels, respectively.

Our simulations were performed by placing a single water molecule close to the nano-rod, as shown in Figure 10. Calculations using the PM5 methodology predict an attractive interaction, with the water molecule physisorbed on the surface of the nano-rod. We then deformed the rod (again with PM5) and the same loading procedure as described in the preceding section. We found three stages of response characterizing the evolution of the reaction with increasing strain, as shown in Figure 10. The first is physisorption of the water molecule (Figure 10a); the water O moves to the vicinity of two Si atoms in a ring without forming a chemical bond. With increasing strain in the nano-rod, this O associates more closely with one of the Si atoms such that above a critical strain, a chemical bond is formed (Figure 10b). At this point, all the stretched Si–O bonds have the same length. This configuration is a metastable state, since both the Si and O are over-coordinated. At a second critical strain, one of the neighboring siloxane bonds breaks to form two stable silanol (Si–OH) groups (Figure 10c). If the hydrolyzed nano-rod is strained further, the entire structure fails through a stress concentration mechanism.
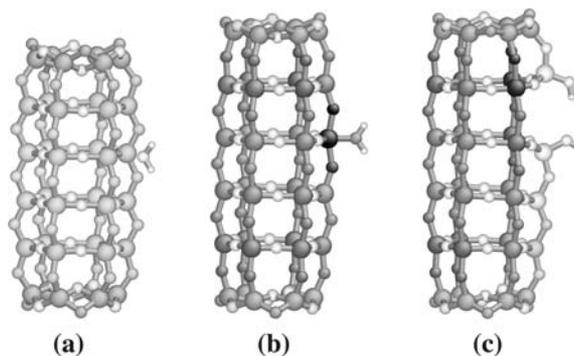

Figure 10. Nano-rod in the presence of water. (a) Position of the physisorbed water molecule, (b) intermediate step and (c) hydrolyzed nano-rod. Strained atoms are plotted in a darker tone.
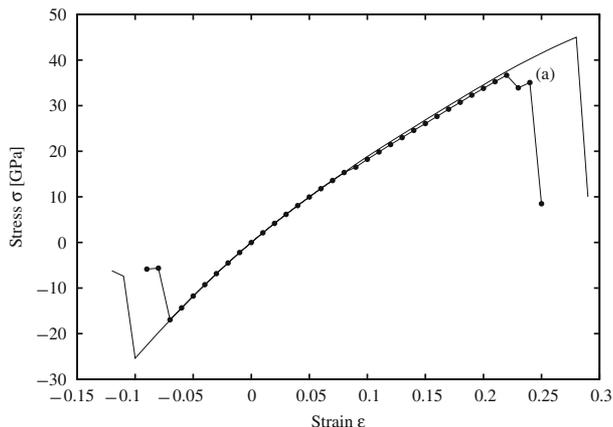
Figure 11. Stress–strain curve for a nano-rod in the presence of water, for the PM5 method. (–) Dry nano-rod and (●) one water molecule. (a) Hydrolyzed nano-rod with one broken bond.

The stress–strain behavior of the wet nano-rod is shown in Figure 11. The overall effect of water is to reduce the critical stress. After hydrolysis, the nano-rod is still able to support stresses, but fails earlier due to the stress redistribution.

Failure of the nano-rod in compression is also enhanced by water. However, we do not go into any details here since the mechanism is not representative of bulk silica.

4.3. DEFORMATION OF A NOTCHED NANO-ROD

As we have seen, the reaction between a water molecule and the silica nano-rod entails two effects. The presence of water reduces the stress needed to break a siloxane bond. Once this bond is broken, stress concentration around the defect site causes a significant reduction in the strength of the hydrolyzed nano-rod. To investigate the two effects separately, we created a notch in the nano-rod by removing an O atom from a siloxane bond (Figure 12), and compared the behavior of the notched and hydrolyzed rods under deformation.
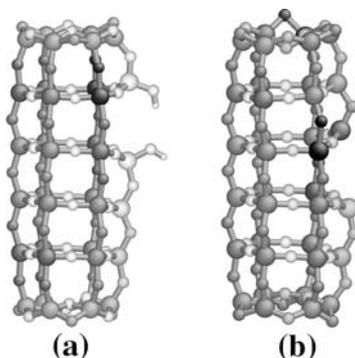

Figure 12. Comparison between a hydrolyzed bond and an artificial notch. (a) Hydrolyzed nano-rod, (b) artificially notched nano-rod. Strained atoms are plotted in a darker tone.
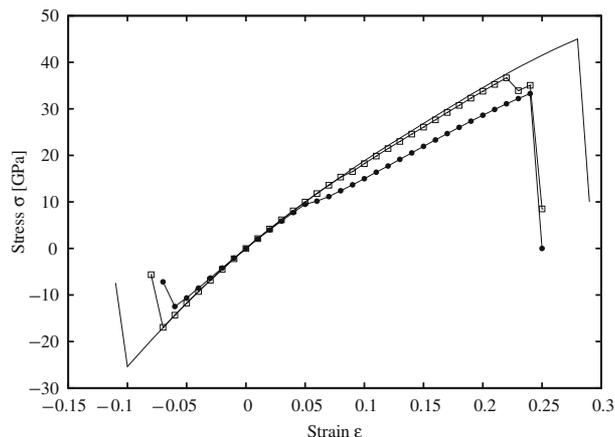
Figure 13. Stress–strain curve for the original and the notched nano-rod in the presence of water, using the PM5 method. (–) dry nano-rod, (□) nano-rod with one water molecule, (●) notched dry nano-rod.

The deformation response of the notched rod is shown in Figure 13. One sees that the hydrolyzed and notched rods are very similar in their critical behavior, with close values for the critical stresses and strains. This comparison suggests that once the water molecule hydrolyzes the nano-rod, the resulting structure is mechanically similar to a notched rod.

4.4. STRESS-DEPENDENT ACTIVATION BARRIER

The most important step in the water–silica reaction is the breaking of the siloxane bond. We now describe an approach to determination of the activation barrier, which in turn depends on the system strain. The basic idea is to apply transition state sampling to obtain the minimum energy path for the reaction. This is tantamount to identifying the reaction coordinates in a system with $3N$ degrees of freedom, with N the number of atoms.

The minimum energy path for hydrolysis of the nano-rod will vary with the imposed strain or stress state, characterized here by the reduced stress, namely σ divided by the critical stress σ_c. The critical stress is defined as that stress value at which the activation barrier disappears and instability occurs spontaneously in a direct simulation. A study of the mechanisms of silica hydrolysis using the NEB method has been reported recently [91, 92]; here we summarize only the most salient findings. The MEP approach has revealed three competing mechanisms for water–silica reactions, each involving a distinct initiation step. The processes are are water dissociation, molecular chemisorption, and direct siloxane bond rupture, which dominate at low, intermediate, and high stress levels, respectively. Among these three, the second mechanism is shown to be the most relevant since it is active in the range where hydrolysis is favorable and the energy barrier is positive.

Figure 14 shows the main steps in the reaction pathway identified using the NEB method while the nano-rod is kept at constant strain. The initial step (Figure 14a) has the water molecule positioned near the nano-rod, under attraction and about to be physisorbed (Figure 14b). The water molecule forms hydrogen bonds with the Os
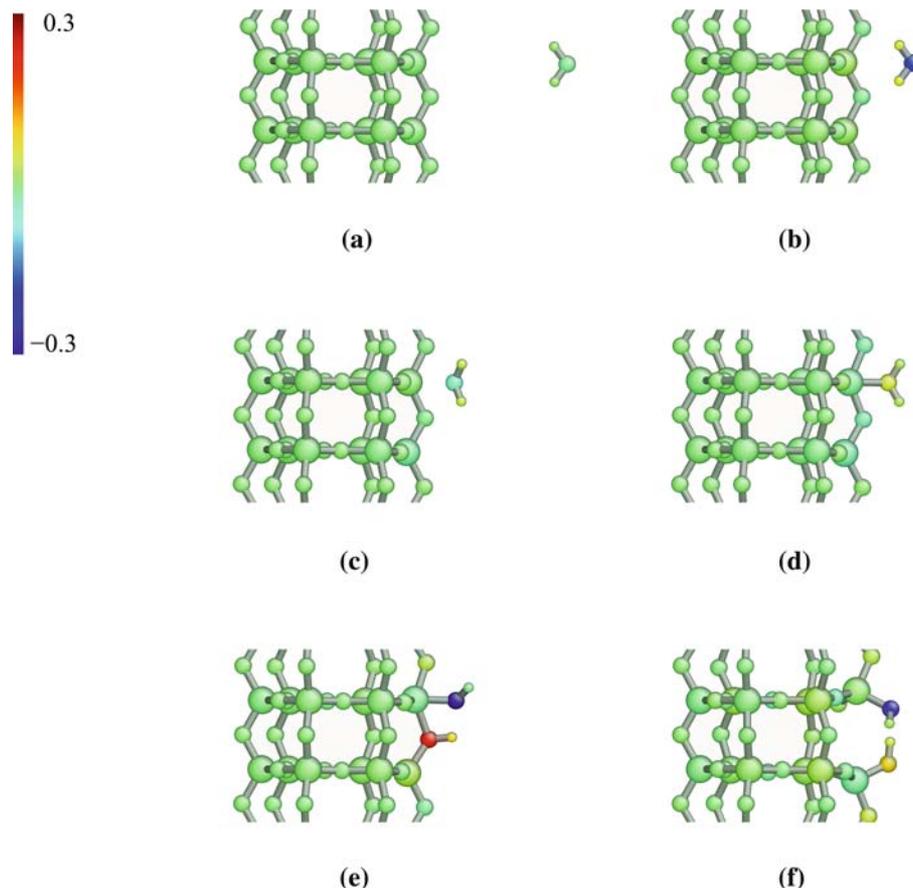
Figure 14. Main steps in the minimum energy path for hydrolysis mechanism II at a stress $\sigma/\sigma_c = 0.3$: (a) initial state, (b) physisorbed state, (c) first saddle point, (d) metastable molecularly adsorbed state, (e) second saddle-point, and (f) hydrolyzed configuration. Atoms are color-coded by charge variation relative to the initial state (a) [92].

in the nano-rod, and some polarization can be observed through the atomic charge. We know from direct simulation that the water O must approach the Si atom to be chemisorbed. However, when below the critical strain, a saddle point (Figure 14c) must be crossed before the chemisorbed state (Figure 14d) is reached. In this metastable state, the Si atom is bonded to five O atoms, a configuration with a low activation barrier for the proton transfer process (Figure 14e), in which a water hydrogen bonds with the O from the broken siloxane bond. Once the transfer occurs, the receiving O atom breaks its bond with the Si atom such that a stable configuration with two silanol groups is formed (Figure 14f).

In the process just described, there are two saddle-points with two activation barriers, as can be seen in the minimum energy path, plotted on Figure 15. Notice that the height of each barrier varies with stress in its own way, consequently the specific limiting step in the reaction is be stress-dependent.

An implication of the present results is that the analysis of energy change with nano-rod bond breaking can help elucidate the thermodynamic driving force of brittle fracture. A current notion in the understanding of brittle fracture at the atomic
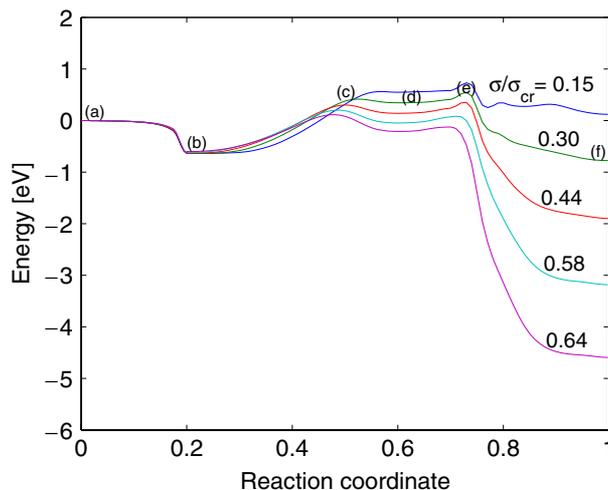
Figure 15. Stress-dependent minimum energy path for the hydrolysis mechanism II. The labels refer to the configurations in Figure 14 [92].

scale is the concept of "lattice trapping", essentially the fracture analog of the Peierls resistance to dislocation motion (see [71]). Consider a simplified model system with an atomically sharp crack embedded in an otherwise perfect 2D lattice. The quasi-static crack growth corresponds to a sequence of localized bond-breaking processes at the instantaneous crack tip. Under a given external load, the total energy of the system can be written as written as a function of crack length. Because of lattice discreteness, the energy landscape is corrugated at the atomic scale along the crack extension direction. Consequently crack extension can stop temporarily when the system is trapped in a local energy well, and an activation energy is required to overcome the local barrier [93]. Each time the crack extends by one lattice spacing, the system will move from one state of local energy minimum to another at the adjacent well. The energy difference between the two local minima states determines the instantaneous thermodynamic driving force for crack extension by one lattice spacing, while the local maximum between the two states defines the activation energy barrier which determines the instantaneous kinetic rate of crack growth. A connection between lattice trapping at a crack tip and bond breaking in a nano-rod can be established if we regard the breaking of a siloxane bond in a perfect nano-rod as effectively creating a small notch crack. The targeted siloxane bond also can be thought of as being lattice trapped. Although the detailed atomic structure and stress state are different for the two situations, we believe that the general trend revealed by the study of the nano-rod bond breaking will be instructive for understanding the hydrolysis reaction at the crack tip [92].

A second implication of our results on water–silica interaction concerns the well-known phenomenon of hydrolytic weakening of quartz [8, 23, 24]. Basically, it was first observed that while synthetic quartz specimens at 300°C have a compressive strength of 2 GPa, at elevated temperatures of 400–600°C the strength dropped rapidly as the specimens plastically deformed significantly without fracture. The interpretation given was that the synthetic crystals contained water which hydrolyzed the silicon–oxygen bonds, forming SiOH groups which became mobile to promote dislocation mobility

[24]. This problem has been investigated actively in the ensuing years [49, 63], with work including molecular calculations at the empirical potential [25, 27] and ab initio [26, 35, 48] levels. It is fair to say that at present the issue of the dominant mechanism for the observed plasticity is still indeterminate. The controversy, stated in admittedly highly simplified manner, seems to lie in deciding which of the two competing candidates, dislocation nucleation versus dislocation mobility, is responsible for the increased dislocation activity seen at elevated temperatures.

5. Outlook

We began this perspective by observing that current recognition of the promise of *computational science* gives urgency to the explicit demonstration of the advantages of the multi-scale modeling and simulation paradigm. In response, we have described a way of systematically probing the chemo-mechanical behavior of silica. We first quantified the theoretical strength of the bulk solid and a nano-rod through the direct simulation of the strain-induced stress response. Then we characterized the stress-assisted reactivity of the nano-rod with a water molecule through transition-state pathway sampling. Besides the specific results and interpretations presented, there is a general implication of this work that we believe to be worthy of comment.

No matter how complex the system under study may be, the fact remains that the structural and dynamical behavior of interest are fundamentally controlled by the underlying energy landscape. It is very likely that details of the landscape for a binary material (SiO_2) are more complicated than those for an elemental substance, such as Cu or Si. Nonetheless, the essential methodology for probing mechanical deformation and chemical reactivity, once established, should be applicable to systems of arbitrary compositional complexity. This is true of the stress–strain curve showing structural instability, or the minimum-energy path, which delineates the activation barrier along with corresponding atomic configurations just prior to instability. From a more general standpoint, we can say that the present multi-scale approach to chemo-mechanics of materials is a hybrid formulation, an attempt toward understanding stress-assisted chemical reactions by focusing on the role of the inter-atomic bond in mechanical deformation as well as chemical bond rupture and formation. We believe the power of this approach lies in the ability of atomistic simulation, whether electron-explicit as in various QM methods, or electron-implicit as in empirical and semi-empirical potential methods, to capture the complexities of bond distortion and charge density redistributions within the constraints of the simulation. Aside from the robustness of the description of inter-atomic interactions, the constraints of atomistic simulations are well-known to be the limited size of the structural features of the material that one can simulate, and the high rate of deformation and reaction that one is forced to observe. Both limitations can be expected to diminish in severity in time, given the continuing increase in computational power and more significantly, the prospects of developing novel techniques to enhance efficiency of phase-space sampling.

In closing we point to a few other complex problems which have a similar chemo-mechanical nature as silica in an aqueous environment. The problem of understanding the high-temperature oxidation of a ceramic is a formidable proto-typical challenge to the modeling of materials in an extreme environment. Oxidation by itself is already certainly a chemical process of fundamental interest. One has, in

addition, to contend with the mechanics of oxygen transport through a very complicated oxide. Another problem of current interest is to establish a reference molecular model of cement. A quantitative description of a system of calcium silicate hydrate, which can be used to interpret a large database of experimental information, is currently lacking. Here a goal would be the eventual understanding of the microscopic factors that influence the shrinkage properties of concrete. Finally, another high-profile area for multi-scale modeling and simulation to play a key role is basic research to support the development of advanced nuclear energy systems. There are a number of challenges and opportunities in both the front and back ends of the nuclear fuel cycle. In the former the problem of environmentally assisted stress corrosion cracking in fuel and cladding materials, which has been studied extensively in experiments, is ripe for computational modeling. In the latter the prediction of nuclear waste migration in various engineered structures, represents perhaps the ultimate problem of rare events. Again, there is chemistry in the process of cation exchange, and mechanics in describing transport over very long time scales. A unique characteristic of nuclear materials, which we have not considered here, is the complexity of radiation damage. This is a problem of rare events in the extreme, in the presence of cation exchange, and the mechanics of transport.

Acknowledgment

References

1. Badro, J. Barrat, J.-L. and Gillet, P., Phys. Rev. Lett., 76(5) (1996) 772.
2. Baëta, R.D. and Ashbee, K.H.G., Phil. Mag., 22 (1970) 625.
3. Baëta, R.D. and Ashbee, K.H.G., Phil. Mag., 22 (1970) 601.
4. Bartlett, R., McClellan, J., Greer, J. and Monaghan, S. J. Comput. Aided Mat. Design, this issue (2006).
5. Benioff, M.R., Lazowska, E.D., et al., Computational science: ensuring America's competitiveness. Report to the President, President's Information Technology Advisory Committee, Washington, DC, June 2005. URL http://www.nitrd.gov/pitac/reports/.
6. Binggeli, N. and Chelikowsky, J.R., Phys. Rev. Lett., 69(15) (1992) 2220.
7. Binggeli, N., Keskar, N.R. and Chelikowsky, J. R. Phys. Rev. B, 49(5) (1994) 3075.
8. Blacic, J.D., Tectonophysics, 27(3) (1975) 271–294.
9. Campañá, C., Müser, M.H., Tse, J.S., Herzbach, D. and Schöffel, P., Phys. Rev. B, 70(22) (2004) 224101.
10. Carter, N.L., Christie, J.M. and Griggs, D.T., J. Geophys. Res., 66 (1961) 2518.
11. Carter, N.L., Christie, J.M. and Griggs, D.T., J. Geol., 72 (1964) 687.
12. Chaplot, S.L. and Sikka, S.K., Phys. Rev. B, 47(10) (1993) 5710.
13. Christie, J.M., Griggs, D.T., and Carter, N.L., J. Geol., 72 (1964) 734.
14. Christie, J.M., Heard, H.C. and LaMori, P. N. Amer. J. Sci. 262 (1964) 26.
15. de Leeuw, N.H., Du, Z.M., Li, J., Yip, S. and Zhu, T., Nano Lett., 3(10) (2003) 1347–1352.
16. Doukhan, J.C., J. Phys. III, 5(11) (1995) 1809–1832.
17. Du, M.H., Kolchin, A. and Cheng, H.P., J. Chem. Phys., 119(13) (2003) 6418–6422.
18. El'Kin, F.S., Brazhkin, V.V., Khvostantsev, L.G., Tsiok, O.B. and Lyapin, A.G., JETP Lett., 75(7) (2002) 342–347.
19. Feuston, B.P. and Garofalini, S.H., J. Chem. Phys., 89(9) (1988) 5818–5824.

20. Gilman, J.J., Electronic Basis of the Strength of Materials, Cambridge University Press, Cambridge, 2003.

21. Ginhoven, R.M.V., Jonsson, H. and Corrales, L.R., Phys. Rev. B, 71(2) (2005) 024208.

22. Ginhoven, R.M.V., Jonsson, H., Park, B. and Corrales, L.R., J. Phys. Chem. B, 109(21) (2005) 10936–10945.

23. Griggs, D., J. Geophys. Res., 79(11) (1974) 1653–1661.

24. Griggs, D. T., Geophys. J. Roy. Astr. S., 14 (1967) 19.

25. Heggie, M. and Jones, R., Philos. Mag. A, 53(5) (1986) L65–L70.

26. Heggie, M. and Jones, R., Philos. Mag. Lett., 55(1) (1987) 47–51.

27. Heggie, M.I., Jones, R., Latham, C.D., Maynard, S.C.P. and Tole, P., Philos. Mag. B, 65(3) (1992) 463–471.

28. Hemley, R.J., In Manghnanin, M.H. and Syono, Y., (Eds.), High-Pressure Research in Mineral Physics, Terra Scientific, Tokyo, 1987.

29. Hemley, R.J., Jephcoat, A.P., Mao, H.K., Ming, L.C. and Manghnani, M.H., Nature, 334(6177) (1988) 52–54.

30. Henkelman, G. and Jónsson, H., J. Chem. Phys., 113(22) (2000) 9978–9985.

31. Hillig, W.B. and Charles, R.J., Surfaces, stress-dependent surface reactions, and strength, In Zackay, V. F. (Ed.), High-Strength Materials, Wiley, New York, 1964, 682–705.

32. Hobbs, B.E., Tectonophysics, 6 (1968) 353.

33. Hobbs, B.E., McLaren, A.C. and Paterson, M.S., Plasticity of single crystals of quartz, In Heard, H.C., Borg, I.Y., Carter, N.L. and Raleigh, C.B., (Eds.), Flow and Fracture of Rocks (The Griggs Volume), Vol. 16 of Geophysical Monograph Series, American Geophysical Union, (1972) 29.

34. Hoover, W.G., Phys. Rev. A, 31(3) (1985) 1695.

35. Jones, R., Oberg, S., Heggie, M.I. and Tole, P., Philos. Mag. Lett., 66(2) (1992) 61–66.

36. Jonsson, H., Mills, G. and Jacobsen, K.W., Nudged elastic band method for finding minimum energy paths of transitions, In Berne, B.J., Ciccotti, G. and Coker, D.F., (Eds.), Classical and Quantum Dynamics in Condensed Phase Simulations, World Scientific, 1998, 385–404.

37. Karasiev, V., Trickey, S.B. and Harris, F., J. Comput. Aided Mat. Design, this issue (2006).

38. Keskar, N.R. and Chelikovsky, J.R., Nature, 358 (1992) 222.

39. Keskar, N.R. and Chelikowsky, J.R., Phys. Rev. B, 48(22) (1993) 16227.

40. Kingma, K.J., Hemley, R.J., Mao, H.K. and Veblen, D.R., Phys. Rev. Lett., 70(25) (1993) 3927–3930.

41. Kingma, K.J., Meade, C., Hemley, R.J., Mao, H.K. and Veblen, D.R., Science, 259(5095) (1993) 666–669.

42. Lacks, D.J., Phys. Rev. Lett., 84(20) (2000) 4629–4632.

43. Laurence, P.R. and Hillier, I.H., Comp. Mat. Sci., 28(1) (2003) 63–75.

44. Lawn, B.R., Fracture of Brittle Solids, 2nd edn., Cambridge University Press, Cambridige, 1993.

45. Liao, D., Atomistic Simulation of Strength and Deformation of Ceramic Materials, PhD thesis, MIT, Cambridge, MA, 2001.

46. Lindsay, C.G., White, G.S., Freiman, S.W. and Wongng, W., J. Am. Ceram. Soc., 77(8) (1994) 2179–2187.

47. Mallik, A., Taylor, D., Runge, K., Dufty, J. and Cheng, H.-P., J. Comput. Aided Mat. Design, this issue (2006).

48. Mcconnell, J.D.C., Phase Transit., 61(1–4) (1997) 19–39.

49. McLaren, A.C., Gerald, J.D.F. and Gerretsen, J., Phys. Chem. Miner., 16(5) (1989) 465–482.

50. McNeil, L.E. and Grimsditch, M., Phys. Rev. Lett., 68(1) (1992) 83–85.

51. Michalske, T. A. and Bunker, B.C., J. Appl. Phys., 56(10) (1984) 2686–2693.

52. Michalske, T.A. and Freiman, S.W., Nature, 295(5849) (1982) 511–512.

53. Michalske, T.A. and Freiman, S.W., J. Am. Ceram. Soc., 66(4) (1983) 284–288.

54. Mukherjee, G.D., Vaidya, S.N. and Sugandhi, V., Phys. Rev. Lett., 87(19) (2001) 195501.

55. Muralidharan, K., Mallik, A., Runge, K. and Deymier, P., J. Comput. Aided Mat. Design, this issue (2006).

56. Muralidharan, K., Simmons, J.H., Deymier, P.A. and Runge, K., J. Non-Cryst. Solids, 351(18) (2005) 1532–1542.

57. Murashov, V.V., Phys. Rev. B, 57(10) (1998) 5639.
58. Nosé, S., Molec. Phys., 52(2) (1984) 255.
59. Ochoa, R., Swiler, T.P. and Simmons, J.H., J. Non-Cryst. Solids, 128 (1991) 57.
60. Oden, J.T., et al. Revolutionizing engineering science through simulation, Report, NSF Blue Ribbon Panel on Simulation-Based Engineering Science, Feb. 2006. URL http://www.ices.utexas.edu/events/SBES_Final_Report.pdf.
61. Oligschleger, C., Phys. Rev. B, 60(5) (1999) 3182.
62. Parrinello, M. and Rahman, A., J. Appl. Phys., 52(12) (1981) 7182.
63. Post, A. and Tullis, J., Tectonophysics, 295 (1998) 117.
64. Saika-Voivod, I., Sciortino, F., Grande, T. and Poole, P.H., Phys. Rev. E, 70(6) (2004) 061507.
65. Sanders, M.J., Leslie, M. and Catlow, C.R.A., J. Chem. Soc. Chem. Comm., (19) (1984) 1271–1273.
66. Stewart, J.J.P., MOPAC 2002 Manual, Fujitsu Ltd., Tokyo, 2002.
67. Subramanian, S., Atomic-level deformation response of SiO_2 under compression, Master's thesis, Massachusetts Institute of Technology, Cambridge, 2001.
68. Subramanian, S. and Yip, S., Comp. Mat. Sci., 23(1–4) (2002) 116–123.
69. Svishchev, I.M., Kusalik, P.G. and Murashov, V.V., Phys. Rev. B, 55(2) (1997) 721.
70. Swiler, T.P., Simmons, J.H. and Wright, A.C., J. Non-Cryst. Solids, 182(1–2) (1995) 68–77.
71. Thomson, R., Hsieh, C. and Rana, V., J. Appl. Phys., 42 (1971) 3145–3160.
72. Trickey, S., Yip, S., Cheng, H.-P., Runge, K. and Deymier, P., J. Comput. Aided Mat. Design, this issue (2006).
73. Tse, J.S. and Klug, D.D., Phys. Rev. Lett., 67(25) (1991) 3559–3562.
74. Tse, J.S. and Klug, D.D., Phys. Rev. Lett., 70(2) (1993) 174–177.
75. Tse, J.S., Klug, D.D. and Allan, D. C., Phys. Rev. B, 51(22) (1995) 16392.
76. Tse, J.S., Klug, D.D., Page, Y.L. and Bernasconi, M., Phys. Rev. B, 56(17) (1997) 10878.
77. Tsuneyuki, S., Matsui, Y., Aoki, H. and Tsukada, M., Nature, 339(6221) (1989) 209–211.
78. Tullis, T.E. and Tullis, J., In Hobbs, B.E. and Heard, H.C., (Eds.), Mineral and Rock Deformation: Laboratory Studies, of AGU Geophysical Monograph, Vol. 39. American Geophysical Union, 1986, 297.
79. Uemura, Y., Phys. Rev. B, 49(10) (1994) 6528.
80. Uemura, Y., Phys. Rev. B, 51(10) (1995) 6704.
81. van Beest, B.W.H., Kramer, G.J. and van Santen, R.A., Phys. Rev. Lett., 64(16) (1990) 1955–1958.
82. Vashishta, P., Kalia, R.K., Rino, J.P. and Ebbsjo, I., Phys. Rev. B, 41(17) (1990) 12197–12209.
83. Vineyard, G.H., J. Phys. Chem. Solids, 3 (1957) 121–127.
84. Walsh, T.R., Wilson, M. and Sutton, A.P., J. Chem. Phys., 113(20) (2000) 9191–9201.
85. Watson, G.W. and Parker, S.C., Phys. Rev. B, 52(18) (1995) 13306.
86. West, J.K. and Hench, L.L., J. Mater. Sci., 29(22) (1994) 5808–5816.
87. Wiederhorn, S.M., J. Am. Ceram. Soc., 50 (1967) 407–414.
88. Wright, A.C., J. Non-Cryst. Solids, 159(3) (1993) 264–268.
89. Yip, S. (Ed.), Handbook of Materials Modeling, Springer, Dordrecht, 2005.
90. Zhu, C., Byrd, R.H. and Nocedal, J., ACM Trans. Math. Softw., 23(4) (1997) 550–560.
91. Zhu, T., Atomistic Characterization of Stress-Driven Configurational Instability and its Activation Mechanisms, PhD thesis, MIT, Cambridge, MA, May 2004.
92. Zhu, T., Li, J., Lin, X. and Yip, S., J. Mech. Phys. Solids, 53(7) (2005) 1597–1623.
93. Zhu, T., Li, J. and Yip, S., Phys. Rev. Lett., 93(20) (2004) 205504.
94. Zhu, T., Li, J., Yip, S., Bartlett, R.J., Trickey, S.B. and de Leeuw, N.H., Mol. Simulat., 29(10–11) (2003) 671–676.
95. Zhu, W., Runge, K. and Trickey, S., J. Comput. Aided Mat. Design, this issue (2006).